

Synthesis, Characterization, and Device Application of Antimony-Substituted Violet Phosphorus: A Layered Material

Franziska Baumer,^{†,‡} Yuqiang Ma,^{‡,‡} Chenfei Shen,^{‡,‡} Anyi Zhang,[‡] Liang Chen,[‡] Yihang Liu,[‡] Daniela Pfister,[†] Tom Nilges,^{*,†} and Chongwu Zhou^{*,‡}

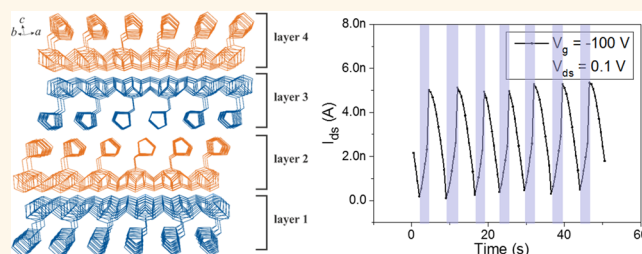
[†]Department für Chemie, Technische Universität München, Lichtenbergstrasse 4, 85747 Garching b. München, Germany

[‡]Department of Electrical Engineering, University of Southern California, 3710 McClintock Avenue, Los Angeles, California 90089-0271, United States

Supporting Information

ABSTRACT: Two-dimensional (2D) nanoflakes have emerged as a class of materials that may impact electronic technologies in the near future. A challenging but rewarding work is to experimentally identify 2D materials and explore their properties. Here, we report the synthesis of a layered material, $P_{20.56(1)}Sb_{0.44(1)}$, with a systematic study on characterizations and device applications. This material demonstrates a direct band gap of around 1.67 eV. Using a laser-cutting method, the thin flakes of this material can be separated into multiple segments. We have also fabricated field effect transistors based on few-layer $P_{20.56(1)}Sb_{0.44(1)}$ flakes with a thickness down to a few nanometers. Interestingly, these field effect transistors show strong photoresponse within the wavelength range of visible light. At room temperature, we have achieved good mobility values (up to $58.96 \text{ cm}^2/\text{V}\cdot\text{s}$), a reasonably high on/off current ratio ($\sim 10^3$), and intrinsic responsivity up to $10 \mu\text{A}/\text{W}$. Our results demonstrate the potential of $P_{20.56(1)}Sb_{0.44(1)}$ thin flakes as a two-dimensional material for applications in visible light detectors.

KEYWORDS: layered material, field effect transistor, antimony-substituted violet phosphorus, photoresponse, mobility



In recent years, 2D materials, including graphene,^{1,2} hexagonal boron nitride (h-BN),^{3,4} transition metal dichalcogenides (TMDCs),^{5–7} black phosphorus (b-P),^{8,9} black arsenic phosphorus (b-AsP),^{10,11} and other compound materials,^{12,13} have attracted significant interest due to their electronic, optical, and mechanical properties. Among these 2D materials, monolayer graphene receives the most attention, which exhibits a zero band gap in its natural state.^{10,14} However, the absence of a band gap in graphene hinders its application as electronic and optoelectronic devices. Another prominent member of the layered materials, h-BN, is an insulator with a large band gap of around 6 eV.^{15,16} Due to its high chemical stability and low conductivity, this material is usually used as hydrophobic substrates or dielectric layers. Another family of 2D layered materials, monolayer TMDCs with the generalized formula MX_2 , have also been reported to present different optical and electrical properties, depending on the number of layers.¹⁷ Recently, b-P and b-AsP, with highly tunable chemical compositions and interesting optical properties, have been reported.^{9,10,18} However, until now, no binary phosphides of Sb and Bi have been reported. Therefore, identifying and exploring the characteristics of these materials, with well-fabricated field

effect transistors (FETs), may lead to potential applications in optoelectronics and nanoelectronics.

Generally speaking, to tune the properties of materials, there are two commonly used methods: substitution and doping. Usually substitution means that the element partially substitutes for another element, forming a stable configuration. For example, it has been shown decades ago that arsenic can be incorporated into b-P under high-pressure treatment.¹⁹ Short-way transport has also been successfully used recently to synthesize black arsenic phosphorus at low-pressure.²⁰ Another material showing the concept of substitution is silicon carbide (SiC), which has been widely used for electronic applications. Light-emitting diodes (LEDs) and detectors made with SiC in early radios were first demonstrated around 1907.²¹ On the other hand, doping technology has been greatly improved in industry, due to the continuous growth and dominance of the complementary metal-oxide–semiconductor (CMOS) technology.²² Doping means the introduction of dopants into the

Received: February 5, 2017

Accepted: March 31, 2017

Published: March 31, 2017

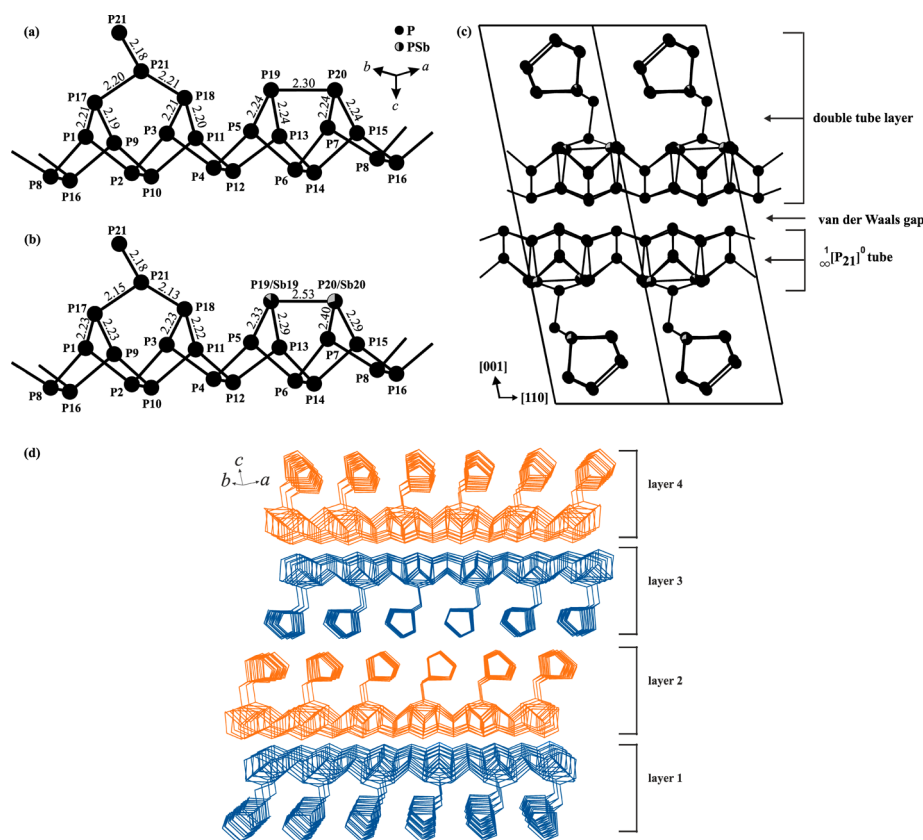


Figure 1. Tubular [P9]P2[P8]P2 substructure of Hittorf's phosphorus and synthesized $P_{20.56(1)}Sb_{0.44(1)}$. Bond lengths are given in Å. (a) Hittorf's phosphorus according to Thurn.³⁰ Bond lengths for P1 to P16 lie in the range of 2.20–2.29 Å. (b) Synthesized PSb with a stoichiometry of $P_{20.56(1)}Sb_{0.44(1)}$. Bond lengths for P1 to P16 are in the range of 2.20–2.29 Å. (c) Crystal structure of Sb-substituted violet or Hittorf's phosphorus $P_{20.56(1)}Sb_{0.44(1)}$. (d) Layered structure of $P_{20.56(1)}Sb_{0.44(1)}$. Four layers are shown, stacked along the *c*-direction.

semiconductor lattice to deliberately change its conductivity because of deficiency or an excess of electrons. In contrast to substitution, doping usually involves elements from multiple groups in the periodic table. Applications of doping technology range from photodetectors,²³ solar cells,²⁴ and low-resistivity semiconductors²⁵ to p–n junctions.²⁶

In this paper, we report the synthesis and characterizations of antimony-substituted violet phosphorus (PSb), $P_{20.56(1)}Sb_{0.44(1)}$, which bears a great resemblance to Hittorf's phosphorus (violet phosphorus),²⁷ with two phosphorus atom positions partially substituted by antimony. The addition of Sb was performed to study how adding substitutional elements would affect the optical and electrical properties of violet phosphorus. This compound formed by P and Sb shows a p-type semiconductor behavior, with decent mobility values. Compared to black arsenic–phosphorus, this material possesses a direct band gap of around 1.67 eV, which can be utilized for photodetectors under visible light. Moreover, during the exfoliation process, these antimony–phosphorus materials show strong in-plane covalent bonding and weak interlayer van der Waals interactions, in accordance with many other 2D materials. The comparison of the title compound, Hittorf's phosphorus, black arsenic–phosphorus, and black phosphorus related to their band gap and mobility values can be found in Table S1.

RESULTS AND DISCUSSION

The synthesis of antimony-substituted violet phosphorus was done by using a lead flux method, with starting material lead, red phosphorus, and antimony sealed in evacuated quartz tubes.

More experimental details on the synthesis of this material can be found in the Methods part. The mixture was heated in a muffle furnace, kept at 770 K for 48 h, then cooled to room temperature. After cooling, antimony-substituted violet phosphorus can be identified in the quartz tubes, since it appears as gray needle-shaped crystals. After exfoliation, flake-like material is obtained and used for further characterization and fabrication. In principle, even monolayer samples can be produced with the exfoliation method; however, finding monolayer samples among a mixture of few layers may not be easy under various microscopes. The main product we obtained, antimony-substituted violet phosphorus, has a structure closely related to Hittorf's phosphorus, with the phosphorus atom substituted by an antimony atom at two positions. The crystal structure of Hittorf's phosphorus consists of tubes with pentagonal cross sections, which are composed of three different subunits. The building units are cages of nine and eight, respectively, phosphorus atoms connected via phosphorus dumbbells. In accordance to the nomenclature of Baudler²⁸ and Häser,²⁹ we can name the ${}^1_{\infty}[P_{21}]^0$ tubes as ${}^1_{\infty}([P9]P2[P8]P2)$. The numbering of the atoms (Figure 1a and b) is analogous to that defined by Thurn.³⁰ The ${}^1_{\infty}[P_{21}]^0$ tubes are perpendicularly connected *via* the roof atom P21 of the [P9] cage to form double tubes. These double-tube layers are stacked along the *c*-direction, only held together *via* van der Waals forces (Figure 1c). A 3-D schematic plot of the layered structure of this material is shown in Figure 1d. The basic unit cell can be repeated in both the *a*-direction and *b*-direction,

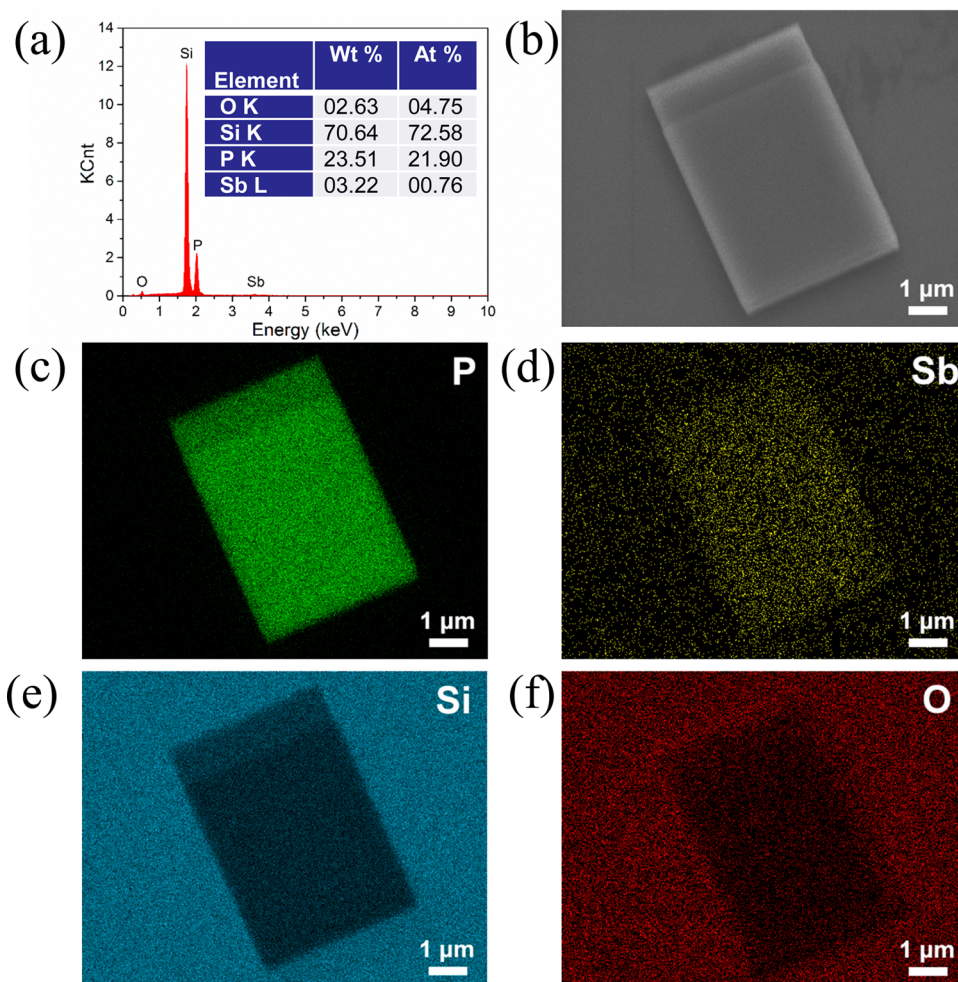


Figure 2. EDX and SEM measurements of a typical PSb thin flake. (a) EDX spectrum of a PSb thin flake. Inset: Elemental analysis of this spectrum measurement. (b) SEM image of the same sample of (a). (c) EDX mapping of element P. (d) EDX mapping of element Sb. (e) EDX mapping of element Si. (f) EDX mapping of element O.

while in the *c*-direction this material shows a typical AB-stacking feature.

The bridge P19–P20 of the [P8] cage is partially occupied with antimony and results in a refined composition of $P_{20.56(1)}Sb_{0.44(1)}$. The bond lengths of P1 to P16 are in the range of 2.20–2.29 Å (Figure S1), which are in perfect agreement with the published bond lengths of Hittorf's phosphorus (2.20–2.29 Å).³¹ In contrast, the substitution of phosphorus with antimony leads to an elongation of the affected bonds, from 2.24 to 2.30 Å in Hittorf's phosphorus to 2.28–2.53 Å in $P_{20.56(1)}Sb_{0.44(1)}$ (Figure 1a and b). The bond length between the mixed occupied sites P19/Sb19 and P20/Sb20 of 2.53 Å (originally 2.29 Å in Hittorf's phosphorus) is clearly enlarged, in comparison to homoatomic P–P bonds, which can be explained by the partial occupancy by antimony on both positions. Sb–Sb bond lengths are 2.91 Å in elemental Sb,³² while the bond lengths of the mixed-occupied sites to the remaining phosphorus skeleton are in the range of 2.29–2.40 Å, which are slightly elongated in contrast to homoatomic P–P bonds (Figure S1). It is also important that the higher the Sb content on P19/Sb19 and P20/Sb20, the larger the deviation from homoatomic P–P bonds observed.

Besides the layered nature of this material, the composition of this material is also worth noting. As verified by energy-dispersive X-ray (EDX) results (Figure 2a), this material

consists of only two elements in group V, *i.e.*, phosphorus and antimony. Interestingly, unlike other layered materials, $P_{20.56(1)}Sb_{0.44(1)}$ thin flakes usually possess rectangular geometry with sharp edges (Figure 2b), which are mostly related to its atomic structures. More scanning electron microscopy (SEM) images of different samples showing this feature can be found in Figure S2. Usually this phenomenon could be observed in materials grown by the chemical vapor deposition (CVD) method, such as MoS_2 or WSe_2 .^{33,34} However, exfoliated layered materials often possess irregular shapes. Compared to CVD-grown materials such as WSe_2 , the exfoliated $P_{20.56(1)}Sb_{0.44(1)}$ thin flakes possess three advantages. First, the surface defects, elemental vacancies, and dangling bonds will be significantly reduced, thus improving the overall quality of the material. Second, the CVD process usually goes through a variation of temperature, which might lead to tensions in chemical bonds caused by expansion or contraction, thus impairing the device performance. Third, CVD-grown materials may have nonuniform distributions or dislocations, depending on the growth thermodynamics.³⁵ From the EDX results shown in Figure 2c–f, we can see that antimony and phosphorus atoms are uniformly distributed in the flake. Therefore, concluded from those advantages mentioned above, the exfoliated $P_{20.56(1)}Sb_{0.44(1)}$ thin flakes would be promising for FET device applications.

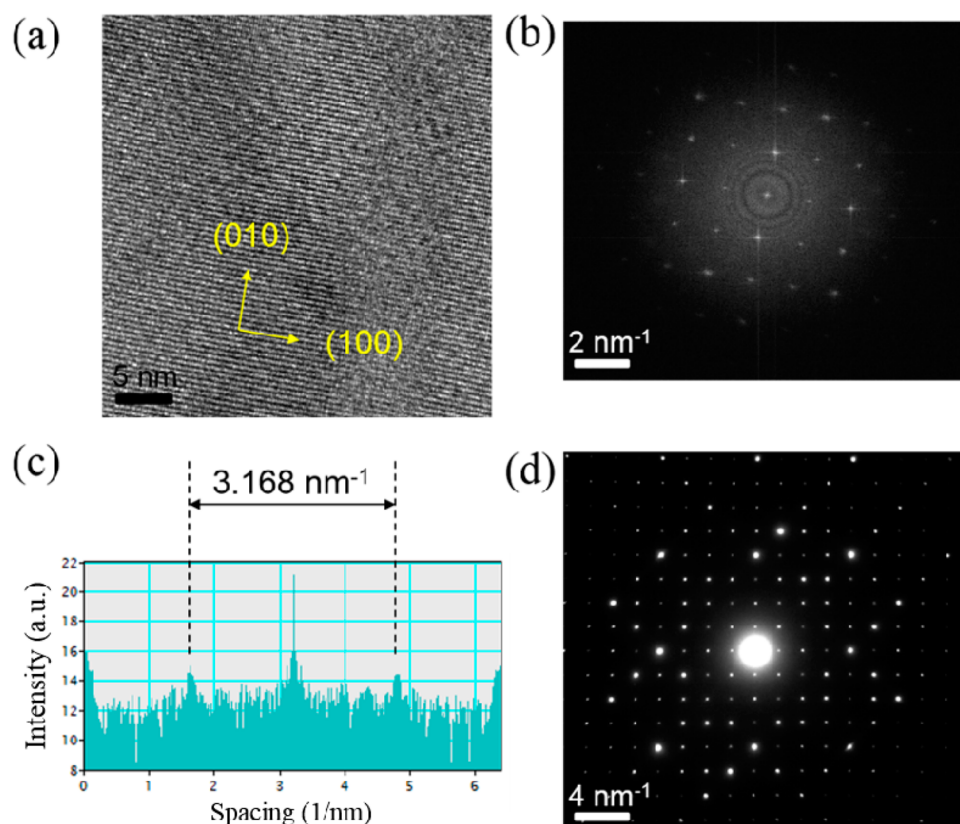


Figure 3. TEM characterization of $P_{20.56(1)}Sb_{0.44(1)}$ thin flakes. (a) High-resolution TEM image of the [001] zone of a PSb thin flake, plane ($hk0$). (b) Reduced FFT image of (a). (c) Profile plot of (b) to measure the planar distance between (100) and $(\bar{1}00)$. (d) Selected area electron diffraction (SAED) pattern of the [001] zone of the PSb thin flake.

A closer scrutiny with transmission electron microscopy (TEM) and powder X-ray diffraction (PXRD) measurements can further reveal features of this material. In Figure 3a, a high-resolution TEM image of synthesized $P_{20.56(1)}Sb_{0.44(1)}$ is given, together with the respective fast Fourier transformation (FFT) in Figure 3b. The planar distance between the continuous lattice fringes shown in Figure 3a is calculated to be 0.631 nm (Figure 3c), in both the (100) and (010) directions. Note that the lattice fringe vector associated with a set of lattice spacing is equal to the reciprocal lattice vector corresponding to the lattice plane set only when this lattice plane set is in exact Bragg condition.³⁶ As reported in the literature, Hittorf's phosphorus possesses a monoclinic crystal structure.³⁷ Here, the selected area electron diffraction (SAED) pattern demonstrates that the PSb thin flake possesses a 2-fold symmetry in the [001] plane (Figure 3d), which is also confirmed by the X-ray diffraction pattern (Figure S3). Coherent with literature reports, our TEM and PXRD results show somewhat comparable lattice parameters to Hittorf's phosphorus. Indexing of the PXRD pattern indicates the lattice parameters to be $a = 9.2345(4) \text{ \AA}$, $b = 9.1732(4) \text{ \AA}$, $c = 22.6176(12) \text{ \AA}$, $\beta = 106.077(4)^\circ$, and $V = 1841.01(16) \text{ \AA}^3$. The structure refinement details of this material are given in Table 1.

In addition to the crystal structure derived from PXRD and TEM results, experimental Raman and photoluminescence (PL) spectral measurements on single crystals of PSb are carried out, aiming at identifying peaks from PSb samples. Due to the low symmetry and 21 different crystallographic atoms in the unit cell, the Raman spectra (Figure 4a) are quite complex, which reveals the existence of multiple vibration modes. The

Table 1. Crystal Data and Structure Refinement for $P_{20.56(1)}Sb_{0.44(1)}$ at $T = 293 \text{ K}$

empirical formula	$P_{20.56(1)}Sb_{0.44(1)}$
space group	$P2/c$ (No. 13)
molar mass/g cm^{-3}	690.3
unit cell dimensions	$a = 9.2345(3) \text{ \AA}$ $b = 9.1732(12) \text{ \AA}$ $c = 22.6176(10) \text{ \AA}$ $\beta = 106.0770(15)^\circ$ $V = 1841.0(2) \text{ \AA}^3$
Z	4
calculated density/g cm^{-3}	2.49
transmission ratio (max/min)	0.7031/0.5400
absorption coefficient/ mm^{-1}	2.46
$F(000)$, e	1323
θ range, deg	4.8–58.5
total number of reflections	18 162
independent reflections	2956 ($R_{\text{int}} = 0.0546$)
reflections with $I \geq 3\sigma(I)$	1413 ($R_\sigma = 0.0604$)
data/parameters	2956/192
goodness-of-fit on F^2	1.10
final R indices [$I \geq 3\sigma(I)$]	$R_1 = 0.0352$ $wR_2 = 0.0608$
R indices (all data)	$R_1 = 0.0833$ $wR_2 = 0.0711$
largest diff. peak and hole/e \AA^{-3}	–0.58/1.13

Raman spectrum of Hittorf's phosphorus has been discussed in the literature, mainly to identify the building units in amorphous red phosphorus.^{37,38} In the Raman spectra shown

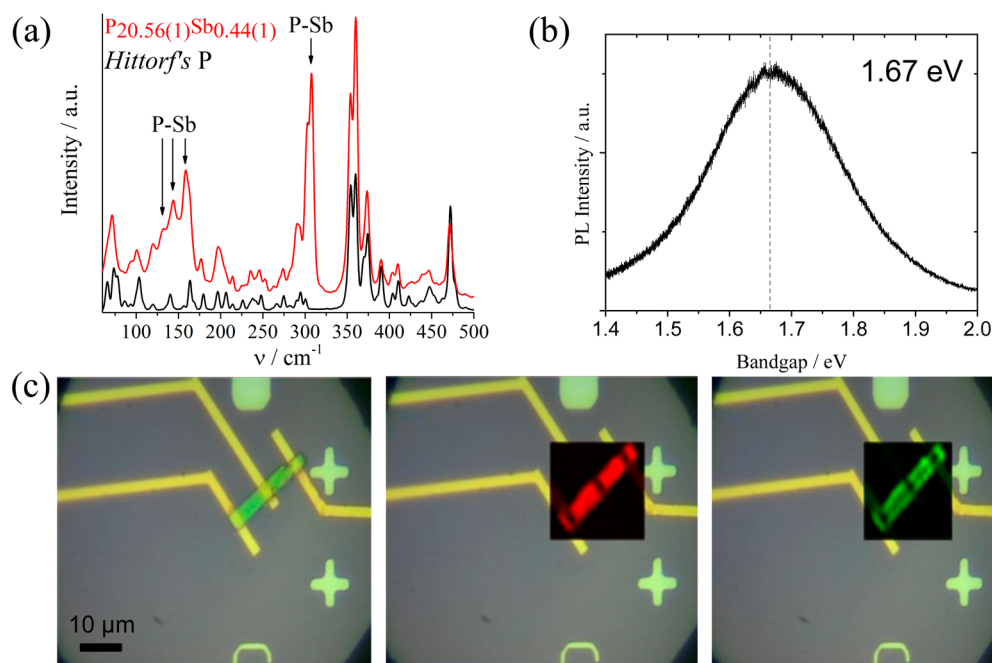


Figure 4. Raman and photoluminescence measurements of PSb. (a) Experimental Raman spectra of single crystals of Hittorf's phosphorus (black line) and PSb (red line). (b) Photoluminescence spectrum of PSb. A direct band gap is observed at ~ 1.67 eV. (c) From left to right: An optical image of a fabricated field effect transistor of PSb; Raman mapping of the flake; photoluminescence mapping of the flake.

in Figure 4a, the peaks could be divided into two groups. Modes above 340 cm^{-1} are induced by intratube vibrations of bond bending and bond stretching. A clear frequency gap between 305 and 350 cm^{-1} is observed, which is a characteristic feature of Hittorf's phosphorus, b-P, and other phosphorus structures.^{37,38} Below 310 cm^{-1} , bond angle distortions, rotational vibration, and extended bending modes are observed.

Intertube and interlayer vibrations contribute to the lower energy range of the spectrum. The Raman spectrum of PSb looks quite similar to that of Hittorf's phosphorus; nevertheless, the most remarkable difference is the additional intense mode at 310 cm^{-1} (indicated by the arrow in Figure 4a), which lies in the postulated "forbidden gap". Neither elemental antimony nor lead shows any bands in this region. Combining the results from single-crystal structure determination and elemental analysis, the 310 cm^{-1} band should be assigned to a P–Sb vibration mode. Also additional peaks at 130 , 145 , and 160 cm^{-1} must be assigned to additional P–Sb stretching or bending modes. In another aspect, the PL spectrum of few-layer PSb demonstrates a direct band gap at around 1.67 eV (Figure 4b). This band gap value is close to monolayer TMDC's band gap, since WSe_2 possesses a direct band gap of around 1.65 eV and MoS_2 around 1.85 eV .^{33,34} Thus, this PSb material should also be capable of showing photoresponse for visible light. Furthermore, we have performed Raman and PL mapping for an as-made FET device (Figure 4c). The Raman mapping is done at 300 cm^{-1} , while the PL mapping is done at 1.67 eV . This thin PSb flake was first exfoliated down to several nanometers in thickness and then transferred onto a Si/SiO₂ wafer. The yellow stripes shown in the optical image are Ti/Au electrodes. Since metal does not present any Raman signals, the Raman mapping at 300 cm^{-1} shows that the P–Sb bonding distributes uniformly in this sample. For the nonuniformity in the PL mapping, there might be several underlying mechanisms, including edge strain, laser-induced defects, and surface absorbates.³⁹ We speculate that the nonuniformity in

the PL mapping mainly comes from edge strain, which might be related to our exfoliation process. Since Raman spectra of PSb are more sensitive to the composition of the material, a uniform Raman intensity map suggests that our PSb sample has a uniform elemental distribution, which is in accordance with the EDX results shown above.

Supplementary to the Raman and PL measurements, we have also observed that a high-power laser can impair the integrity of the PSb samples, as shown in Figure 5. After 10 s of fully powered 532 nm laser exposure, the PSb sample vanishes at the very point of laser illumination, which proves that PSb is not

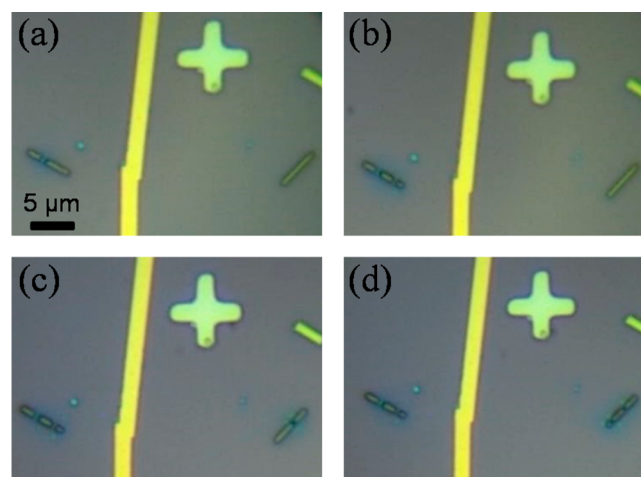


Figure 5. Degradation of exfoliated $\text{P}_{20.56(1)}\text{Sb}_{0.44(1)}$ under 532 nm laser exposure. The laser power is set to be 0.5 W/s . Disappearance of the original material can be clearly observed. (a–d) Optical images after different times of laser exposure. The time interval for each 532 nm laser exposure is 10 s . The cross and the stripe in the images are used for alignment, indicating the consistency of locations.

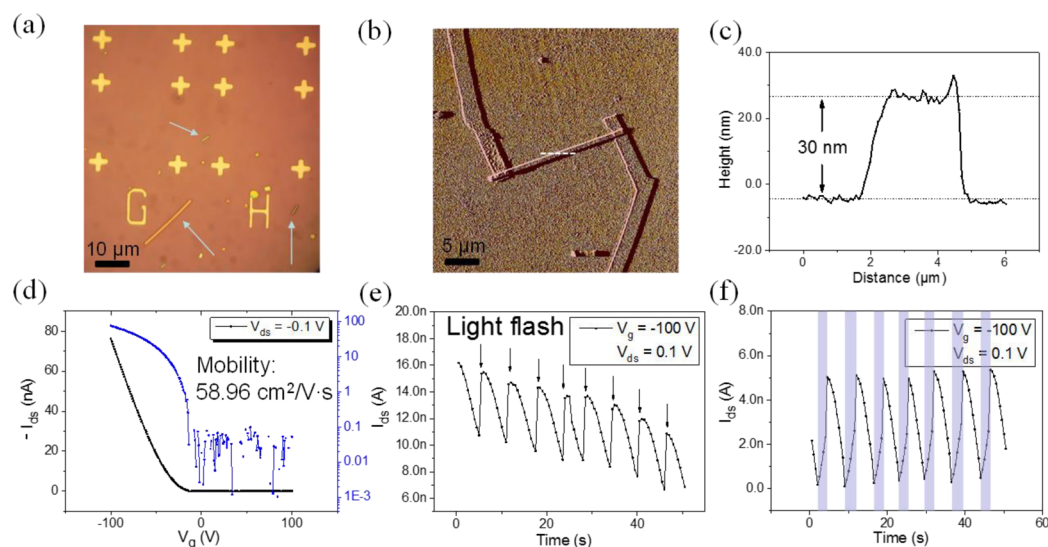


Figure 6. Photodetector made by an exfoliated few-layer PSb flake. (a) Optical image of the exfoliated PSb thin flakes. Multiple flakes are pointed out by arrows in the image. (b) Atomic force microscopy (AFM) image of one as-made FET device. (c) Profile plot of the AFM image in (b), showing that the thickness of the PSb flake is around 30 nm. (d) I_{ds} - V_g curve of the FET shown in (b). The mobility value is calculated to be $58.96 \text{ cm}^2/\text{V}\cdot\text{s}$. (e) I_{ds} vs time curve of a photodetector device made with PSb. The arrows indicate when the light flashes. (f) I_{ds} vs time curve of another photodetector device made with PSb. In the purple regions the light is turned on, while in other regions the light is turned off.

stable under extreme laser conditions. During the laser-cutting experiment, we first cut the sample on the left into three segments and then cut the right one into three segments as well (shown in Figure 5a–d). As can be seen from the images, the spot size is around $0.5 \mu\text{m}$, which can be treated as a fine operation of the flake. This laser-cutting method could be used to separate the PSb samples into desired sizes and shapes, which may benefit the scalable integrated circuit with uniform-sized samples. Notably, the PSb thin flakes do not show signs of degradation under lab conditions (room temperature, atmosphere surrounding), which is distinct from the behavior of black arsenic phosphorus. The instability of PSb under strong laser elimination may be related to oxidation of phosphorus, resulting in phosphorus oxide, which will quickly sublime into the environment. Here again we find the PSb thin flakes are in regular shapes with sharp edges. Thus, by combining the laser-cutting and the sharp edges, we can easily achieve all kinds of shapes with a predefined laser-cutting path.

Since we have shown that PSb has a direct band gap and strong response to light in a certain wavelength range, we have further fabricated photodetectors with PSb as the channel material. We start with the bulk material and then exfoliate PSb down to thin flakes. Notably, PSb thin flakes keep a rectangular or needle-like shape after exfoliation (Figure 6a), which has been discussed earlier. This facilitates the fabrication of FETs since the channel lengths and widths are naturally defined. A typical atomic force microscopy (AFM) image of an as-made FET device is shown in Figure 6b, and the profile plot in Figure 6c verifies that the thickness is around 30 nm. Compared to its lateral size, which is micrometer scale, this material shows a flat surface, corresponding to its layered nature. For this FET device, the optical and SEM images are also available in the Supporting Information (Figure S4). As shown in the images, the channel width of this device is $0.8 \mu\text{m}$, while the channel length is $20.4 \mu\text{m}$. The dielectric is 300 nm SiO_2 above the silicon back gate. We observe that the I_{ds} - V_g curve of this FET shows a p-type transistor behavior for PSb (Figure 6d).

Remarkably, the mobility value is calculated to be $58.96 \text{ cm}^2/\text{V}\cdot\text{s}$, with a reasonable on-state current of 75.21 nA under a source–drain voltage that is set to be -0.1 V . Hence, the normalized two-probe resistivity is calculated to be $1.06 \text{ M}\Omega\cdot\mu\text{m}$. Compared to undoped TMDC materials, the mobility and conductivity values of PSb substantially overwhelm MoS_2 and WSe_2 grown by the CVD method, since the exfoliated PSb samples are free from defects induced by CVD growth.^{6,34} Also the on/off ratio is around 10^3 , with a noise level near 10 – 100 pA . We also measured I_{ds} - V_{ds} family curves for this device (Figure S5). Additionally, we fabricated photodetectors with similar structure to our FET devices (the fabrication details can be found in the Methods part). Visible cold light (broad wavelength spectrum and a spot size of $\sim 1 \text{ mm}$) is used for the measurement of photoresponse. Figure 6e and f are obtained by two other devices, which show two different kinds of measurements: the former one uses a flashing light that will flash every 6 s, while the latter one uses a light source that is continuously switched on and off. It can be observed that the shining light will boost the electric conductivity significantly. The current increase can vary from 1.5 times to ~ 100 times after exposure to different light sources. Different devices would show different boosting ratios, but their behaviors under light/dark transition are similar. Overall, these results are indicative of the potential of PSb as a promising material for visible light detection.

CONCLUSION

In conclusion, we have demonstrated the synthesis, structural characterization, and electronic device application for a layered material, $\text{P}_{20.56(1)}\text{Sb}_{0.44(1)}$. Sb substitution on two distinct sites leads to an enlargement of the bond lengths in this local area. Raman spectroscopy, EDX, TEM, and PXRD results are provided to reveal the crystal structure details of this material. Also we have shown that this material possesses a direct band gap at around 1.67 eV , which leads us to fabricate photodetectors under visible light with exfoliated PSb thin flakes. We

also look into the stability of this material under extreme laser conditions and find that the laser-cutting method can be utilized to reshape the PSb flakes. Furthermore, we have fabricated FET devices. The mobility value ($58.96 \text{ cm}^2/\text{V}\cdot\text{s}$), resistivity value ($1.06 \text{ M}\Omega\cdot\mu\text{m}$), and the on/off ratio (10^3) of PSb are reasonably inspiring, compared to those values of TMDC materials. These results further suggest that antimony-substituted violet phosphorus could be a promising candidate for visible light sensing applications.

METHODS

Synthesis of Antimony-Substituted Violet Phosphorus. The samples were prepared *via* a lead flux, as described for pure violet phosphorus in the literature.^{30,31,40} We slightly modified the standard procedure by adding antimony to the Pb:P mixture. A detailed description of the adapted synthesis is given: Pieces of lead (Fluka, 99.9999%), red phosphorus (CHEMPUR, 99.99999%), and antimony (CHEMPUR, 99.99999%) were used, and the starting materials of total weight of 300 mg were sealed in evacuated quartz tubes. The mixture was first heated in a muffle furnace for 10 h, ramping up to 770 K. After that the temperature was kept at 770 K for 48 h. Then the furnace was cooled to room temperature using a ramp of 3 K/h. The product was derived from a ratio of Pb:P:Sb = 1:5:2 and could be found either on top of the molten lead or on the inner surface of the ampule, as bundles of fine needles. Variations of the starting composition (*e.g.*, the increase of the lead content) and temperature led to similar results. Besides the lead remaining, we also found antimony crystals as a side product, which could be easily separated from the main product (Figure S6). Subject to phase analysis, the needle-shaped crystals were identified as phase-pure Sb-substituted violet phosphorus.

X-ray Diffraction. Powder X-ray diffraction measurements were carried out on a STOE Stadi P diffractometer (Cu $K\alpha_1$ radiation, $\lambda = 1.54051 \text{ \AA}$; germanium monochromator) in transmission mode with a flatbed sample holder. Data analysis was carried out with the program package WinXPOW.⁴¹ Determined lattice parameters were further used for the single-crystal structure refinement.

Single-crystal intensity spectra were obtained at room temperature using a STOE IPDS-II diffractometer (Mo $K\alpha$ radiation; $\lambda = 0.71073 \text{ \AA}$; graphite monochromator), on which a numerical absorption correction was applied. Structure simulation and refinement (full matrix, least-squares on F^2) has been performed with Superflip,⁴² which is embedded in the program Jana 2006,⁴³ where 21 maxima of electron density were initially assigned to phosphorus. P1–P18 and P21 were fully occupied within the 3-fold standard deviation, and the site occupancy factor (SOF) was set to 1 during refinement. Due to the elongated bond length and significantly smaller atomic displacement values, P19 and P20 were identified as mixed P/Sb occupied sites restricted to an overall SOF of 1. The obtained refined composition of $\text{P}_{20.56(1)}\text{Sb}_{0.44(1)}$ is in good agreement with the EDX data. Crystallographic data such as refined atomic positions, displacement parameters, and interatomic distances of $\text{P}_{20.56(1)}\text{Sb}_{0.44(1)}$ are given in Tables 1 and S2–S4. Further structure refinement details may be obtained from Fachinformationszentrum Karlsruhe (D-76344 Eggenstein-Leopoldshafen) by quoting the registry number CSD-432344.

Scanning Electron Microscope and EDX Data. Semiquantitative EDX analyses of single crystals were carried out by using a JEOL JCM-6000 scanning electron microscope with a JED 2200 detector in high-vacuum mode and an acceleration voltage of 15 kV. Impurities heavier than sodium could not be detected in our samples. A composition of P:Sb 98(1):2(1) was derived by averaging more than 30 measurements of different crystals. Lead was not found in any of the crystals in significant amounts. A field emission scanning electron microscope (JEOL JSM-7001) equipped with an EDX system was used for SEM images and EDX mapping of PSb thin flakes.

Raman and Photoluminescence Spectroscopy. Several single crystals were investigated by Raman spectroscopy measurements with a Senterra spectrometer of Bruker Optics GMBH equipped with a 785

nm laser and an applied power of 1 mW. Photoluminescence measurement was carried out with Renishaw Raman spectroscopy (532 nm laser, 15 mW). Raman and photoluminescence mapping were performed with 1% laser power (Renishaw Raman spectroscopy, 532 nm laser) in ambient conditions.

AFM Characterization. AFM (DI 3100 Digital Instruments) scanning was performed on PSb thin flakes to determine the height of the material. Both the phase and height images have a resolution of 512×512 . The scanning was done in ambient conditions. No degradation of PSb under lab conditions was detected. A comparison of AFM measurements with a separation time of 1 month can be found in Figure S7.

Antimony-Substituted Violet Phosphorus Device Fabrication and Measurements. The PSb material was first exfoliated by using vacuum tape (Kapton Tapes). After exfoliation, the sample was transferred onto Si/SiO₂ substrates (the thickness of SiO₂ is 300 nm), followed by rinsing and residue-removing procedures. A bilayer of poly(methyl methacrylate) (PMMA) was then spin-coated onto the Si/SiO₂ surface. After spin-coating, electron beam lithography was conducted to pattern the source/drain electrodes, followed by development, metal deposition, and lift-off processes. Ti/Au electrodes (3 nm/30 nm) were deposited at 7×10^{-7} Torr using an e-beam evaporator. The device measurements were performed using an Agilent 4156B in ambient conditions.

For photodetector measurements, cold light sources of halogens are used (HL150-AY). The light source is commercially available, and the spectrum coverage is equivalent to 3200 K lamp color temperature.

The field effect mobility value of PSb FETs was calculated using the following equation:

$$\mu = \frac{L}{W} \frac{1}{C_{\text{ox}} V_{\text{ds}}} \frac{dI_{\text{ds}}}{dV_{\text{g}}}$$

where L and W are the channel length and width of the FET. V_{ds} stands for the source–drain voltage, while I_{ds} stands for the current flowing from source to drain. V_{g} is the applied back-gate voltage. C_{ox} is the gate capacitance per unit area.

ASSOCIATED CONTENT

Supporting Information

The Supporting Information is available free of charge on the ACS Publications website at DOI: 10.1021/acsnano.7b00798.

SEM, XRD, optical images, I – V measurements, AFM measurements, and tables of crystal structure parameters of antimony-substituted violet phosphorus (PDF)

AUTHOR INFORMATION

Corresponding Authors

*E-mail: tom.nilges@lrz.tum.de.

*E-mail: chongwuz@usc.edu.

ORCID

Yihang Liu: 0000-0002-2491-9439

Chongwu Zhou: 0000-0001-8448-8450

Author Contributions

*F. Baumer, Y. Ma, and C. Shen contributed equally to this work.

Notes

The authors declare no competing financial interest.

ACKNOWLEDGMENTS

This work is financially supported by the Technische Universität München Graduate School and King Abdulaziz City for Science and Technology (KACST). We acknowledge Stephen Cronin of University of Southern California for access to the Raman facility. We also acknowledge the Center for

Electron Microscopy and Microanalysis of University of Southern California for access to SEM and TEM facilities.

REFERENCES

- (1) Novoselov, K. S.; Geim, A. K.; Morozov, S. V.; Jiang, D.; Zhang, Y.; Dubonos, S. V.; Grigorieva, I. V.; Firsov, A. A. Electric Field Effect in Atomically Thin Carbon Films. *Science* **2004**, *306*, 666–669.
- (2) Novoselov, K. S.; Geim, A. K.; Morozov, S. V.; Jiang, D.; Katsnelson, M. I.; Grigorieva, I. V.; Dubonos, S. V.; Firsov, A. A. Two-Dimensional Gas of Massless Dirac Fermions in Graphene. *Nature* **2005**, *438*, 197–200.
- (3) Novoselov, K. S.; Jiang, D.; Schedin, F.; Booth, T. J.; Khotkevich, V. V.; Morozov, S. V.; Geim, A. K. Two-Dimensional Atomic Crystals. *Proc. Natl. Acad. Sci. U. S. A.* **2005**, *102*, 10451–10453.
- (4) Coleman, J. N.; Lotya, M.; O'Neill, A.; Bergin, S. D.; King, P. J.; Khan, U.; Young, K.; Gaucher, A.; De, S.; Smith, R. J.; Shvets, I. V.; Arora, S. K.; Stanton, G.; Kim, H. Y.; Lee, K.; Kim, G. T.; Duesberg, G. S.; Hallam, T.; Boland, J. J.; Wang, J. J.; et al. Two-Dimensional Nanosheets Produced by Liquid Exfoliation of Layered Materials. *Science* **2011**, *331*, 568–571.
- (5) Najmaei, S.; Liu, Z.; Zhou, W.; Zou, X. L.; Shi, G.; Lei, S. D.; Yakobson, B. I.; Idrobo, J. C.; Ajayan, P. M.; Lou, J. Vapour Phase Growth and Grain Boundary Structure of Molybdenum Disulfide Atomic Layers. *Nat. Mater.* **2013**, *12*, 754–759.
- (6) Ma, Y. G.; Liu, B. L.; Zhang, A. Y.; Chen, L.; Fathi, M.; Shen, C. F.; Abbas, A. N.; Ge, M. Y.; Mecklenburg, M.; Zhou, C. W. Reversible Semiconducting-to-Metallic Phase Transition in Chemical Vapor Deposition Grown Monolayer WSe₂ and Applications for Devices. *ACS Nano* **2015**, *9*, 7383–7391.
- (7) Wang, Q. H.; Kalantar-Zadeh, K.; Kis, A.; Coleman, J. N.; Strano, M. S. Electronics and Optoelectronics of Two-Dimensional Transition Metal Dichalcogenides. *Nat. Nanotechnol.* **2012**, *7*, 699–712.
- (8) Guo, Q. S.; Pospischil, A.; Bhuiyan, M.; Jiang, H.; Tian, H.; Farmer, D.; Deng, B. C.; Li, C.; Han, S. J.; Wang, H.; Xia, Q. F.; Ma, T. P.; Mueller, T.; Xia, F. N. Black Phosphorus Mid-Infrared Photodetectors with High Gain. *Nano Lett.* **2016**, *16*, 4648–4655.
- (9) Li, L. K.; Yu, Y. J.; Ye, G. J.; Ge, Q. Q.; Ou, X. D.; Wu, H.; Feng, D. L.; Chen, X. H.; Zhang, Y. B. Black Phosphorus Field-Effect Transistors. *Nat. Nanotechnol.* **2014**, *9*, 372–377.
- (10) Liu, B. L.; Köpf, M.; Abbas, A. N.; Wang, X. M.; Guo, Q. S.; Jia, Y. C.; Xia, F. N.; Wehrich, R.; Bachhuber, F.; Pielhofer, F.; Wang, H.; Dhall, R.; Cronin, S. B.; Ge, M. Y.; Fang, X.; Nilges, T.; Zhou, C. W. Black Arsenic-Phosphorus: Layered Anisotropic Infrared Semiconductors with Highly Tunable Compositions and Properties. *Adv. Mater.* **2015**, *27*, 4423–4429.
- (11) Xie, M. Q.; Zhang, S. L.; Cai, B.; Huang, Y.; Zou, Y. S.; Guo, B.; Gu, Y.; Zeng, H. B. A Promising Two-Dimensional Solar Cell Donor: Black Arsenic-Phosphorus Monolayer with 1.54 eV Direct Bandgap and Mobility Exceeding 14,000 cm² V⁻¹ s⁻¹. *Nano Energy* **2016**, *28*, 433–439.
- (12) Carey, B. J.; Ou, J. Z.; Clark, R. M.; Berean, K. J.; Zavabeti, A.; Chesman, A. S. R.; Russo, S. P.; Lau, D. W. M.; Xu, Z.-Q.; Bao, Q.; Kevehei, O.; Gibson, B. C.; Dickey, M. D.; Kaner, R. B.; Daeneke, T.; Kalantar-Zadeh, K. Wafer-Scale Two-Dimensional Semiconductors from Printed Oxide Skin of Liquid Metals. *Nat. Commun.* **2017**, *8*, 14482.
- (13) Kalantar-zadeh, K.; Ou, J. Z.; Daeneke, T.; Mitchell, A.; Sasaki, T.; Fuhrer, M. S. Two Dimensional and Layered Transition Metal Oxides. *Appl. Mater. Today* **2016**, *5*, 73–89.
- (14) Zhang, Y. B.; Tang, T. T.; Girit, C.; Hao, Z.; Martin, M. C.; Zettl, A.; Crommie, M. F.; Shen, Y. R.; Wang, F. Direct Observation of a Widely Tunable Bandgap in Bilayer Graphene. *Nature* **2009**, *459*, 820–823.
- (15) Lin, Y.; Connell, J. W. Advances in 2D Boron Nitride Nanostructures: Nanosheets, Nanoribbons, Nanomeshes, and Hybrids with Graphene. *Nanoscale* **2012**, *4*, 6908–6939.
- (16) Kubota, Y.; Watanabe, K.; Tsuda, O.; Taniguchi, T. Deep Ultraviolet Light-Emitting Hexagonal Boron Nitride Synthesized at Atmospheric Pressure. *Science* **2007**, *317*, 932–934.
- (17) Kim, K. K.; Hsu, A.; Jia, X. T.; Kim, S. M.; Shi, Y. M.; Dresselhaus, M.; Palacios, T.; Kong, J. Synthesis and Characterization of Hexagonal Boron Nitride Film as a Dielectric Layer for Graphene Devices. *ACS Nano* **2012**, *6*, 8583–8590.
- (18) Liu, H.; Neal, A. T.; Zhu, Z.; Luo, Z.; Xu, X. F.; Tomanek, D.; Ye, P. D. Phosphorene: An Unexplored 2D Semiconductor with a High Hole Mobility. *ACS Nano* **2014**, *8*, 4033–4041.
- (19) Shirovani, I.; Mikami, J.; Adachi, T.; Katayama, Y.; Tsuji, K.; Kawamura, H.; Shimomura, O.; Nakajima, T. Phase-Transitions and Superconductivity of Black Phosphorus and Phosphorus Arsenic Alloys at Low-Temperatures and High-Pressures. *Phys. Rev. B: Condens. Matter Mater. Phys.* **1994**, *50*, 16274–16278.
- (20) Osters, O.; Nilges, T.; Bachhuber, F.; Pielhofer, F.; Wehrich, R.; Schöneich, M.; Schmidt, P. Synthesis and Identification of Metastable Compounds: Black Arsenic—Science or Fiction. *Angew. Chem., Int. Ed.* **2012**, *51*, 2994–2997.
- (21) Dunwoody, H. H. C. Wireless-Telegraph System. Patent, US 837616 A, 1906.
- (22) O'Brien, S. C. The Chemistry of the Semiconductor Industry. *Chem. Soc. Rev.* **1996**, *25*, 393–400.
- (23) Xiang, D.; Han, C.; Wu, J.; Zhong, S.; Liu, Y. Y.; Lin, J. D.; Zhang, X. A.; Hu, W. P.; Ozyilmaz, B.; Neto, A. H. C.; Wee, A. T. S.; Chen, W. Surface Transfer Doping Induced Effective Modulation on Ambipolar Characteristics of Few-Layer Black Phosphorus. *Nat. Commun.* **2015**, *6*, 648510.1038/ncomms7485.
- (24) Bullock, J.; Hettick, M.; Geissbühler, J.; Ong, A. J.; Allen, T.; Sutter-Fella, Carolin, M.; Chen, T.; Ota, H.; Schaler, E. W.; De Wolf, S.; Ballif, C.; Cuevas, A.; Javey, A. Efficient Silicon Solar Cells with Dopant-Free Asymmetric Heterocontacts. *Nature Energy* **2016**, *1*, 15031.
- (25) McDonnell, S.; Addou, R.; Buie, C.; Wallace, R. M.; Hinkle, C. L. Defect-Dominated Doping and Contact Resistance in MoS₂. *ACS Nano* **2014**, *8*, 2880–2888.
- (26) Buscema, M.; Groenendijk, D. J.; Steele, G. A.; van der Zant, H. S. J.; Castellanos-Gomez, A. Photovoltaic Effect in Few-Layer Black Phosphorus PN Junctions Defined by Local Electrostatic Gating. *Nat. Commun.* **2014**, *5*, 4651.
- (27) Schusteritsch, G.; Uhrin, M.; Pickard, C. J. Single-Layered Hittorf's Phosphorus: A Wide-Bandgap High Mobility 2D Material. *Nano Lett.* **2016**, *16*, 2975–2980.
- (28) Baudler, M.; Glinka, K. Contributions to the Chemistry of Phosphorus. 218. Monocyclic and Polycyclic Phosphines. *Chem. Rev.* **1993**, *93*, 1623–1667.
- (29) Böcker, S.; Häser, M. Covalent Structures Of Phosphorus - a Comprehensive Theoretical Study. *Z. Anorg. Allg. Chem.* **1995**, *621*, 258–286.
- (30) Thurn, H.; Krebs, H. Über Struktur und Eigenschaften der Halbmetalle. XXII. Die Kristallstruktur des Hittorfschen Phosphors. *Acta Crystallogr., Sect. B: Struct. Crystallogr. Cryst. Chem.* **1969**, *25*, 125–135.
- (31) Hittorf, W. *Ann. Phys.* **1865**, *4*, 193.
- (32) Donohue, J. *The Structures of the Elements*, 2nd ed.; Wiley: New York, 1982; p 307.
- (33) Liu, B. L.; Chen, L.; Liu, G.; Abbas, A. N.; Fathi, M.; Zhou, C. W. High-Performance Chemical Sensing Using Schottky-Contacted Chemical Vapor Deposition Grown Monolayer MoS₂ Transistors. *ACS Nano* **2014**, *8*, 5304–5314.
- (34) Liu, B. L.; Fathi, M.; Chen, L.; Abbas, A.; Ma, Y. Q.; Zhou, C. W. Chemical Vapor Deposition Growth of Monolayer WSe₂ with Tunable Device Characteristics and Growth Mechanism Study. *ACS Nano* **2015**, *9*, 6119–6127.
- (35) Chen, L.; Liu, B. L.; Abbas, A. N.; Ma, Y. Q.; Fang, X.; Liu, Y. H.; Zhou, C. W. Screw-Dislocation-Driven Growth of Two-Dimensional Few-Layer and Pyramid-like WSe₂ by Sulfur-Assisted Chemical Vapor Deposition. *ACS Nano* **2014**, *8*, 11543–11551.
- (36) W, Q. Direct Space (Nano)Crystallography Via High-Resolution Transmission-Electron Microscopy. A Dissertation Presented to the Faculty of the Graduate School of the University of

Missouri-Rolla, A Dissertation Presented to the Faculty of the Graduate School of the University Of Missouri-Rolla2000.

(37) Fasol, G.; Cardona, M.; Hönlé, W.; von Schnering, H. G. Lattice Dynamics of Hittorf's Phosphorus and Identification of Structural Groups and Defects in Amorphous Red Phosphorus. *Solid State Commun.* **1984**, *52*, 307–310.

(38) Olego, D. J.; Baumann, J. A.; Kuck, M. A.; Schachter, R.; Michel, C. G.; Raccah, P. M. The Microscopic Structure of Bulk Amorphous Red Phosphorus: A Raman Scattering Investigation. *Solid State Commun.* **1984**, *52*, 311–314.

(39) Peimyoo, N.; Shang, J. Z.; Cong, C. X.; Shen, X. N.; Wu, X. Y.; Yeow, E. K. L.; Yu, T. Nonblinking, Intense Two-Dimensional Light Emitter: Monolayer WS₂ Triangles. *ACS Nano* **2013**, *7*, 10985–10994.

(40) Böcker, S.; Häser, M. Covalent Structures of Phosphorus: A Comprehensive Theoretical Study. *Z. Anorg. Allg. Chem.* **1995**, *621*, 258–286.

(41) *WinXpov* (version 3.0.2.1), S. C. G., Darmstadt, Germany, 2011.

(42) Palatinus, L.; Chapuis, G. SUPERFLIP - A Computer Program for the Solution of Crystal Structures by Charge Flipping in Arbitrary Dimensions. *J. Appl. Crystallogr.* **2007**, *40*, 786–790.

(43) Petříček, V.; Dušek, M.; Palatinus, L. Crystallographic Computing System JANA2006: General Features. *Z. Kristallogr. - Cryst. Mater.* **2014**, *229*, 345–352.